

Identification of patterns in cosmic-ray arrival directions using dynamic graph convolutional neural networks

T. Bister, M. Erdmann*, J. Glombitza, N. Langner, J. Schulte, M. Wirtz

III. Physikalisches Institut A, RWTH Aachen University, Otto-Blumenthal-Str., 52056 Aachen, Germany

ARTICLE INFO

Article history:

Received 30 March 2020

Revised 17 September 2020

Accepted 6 October 2020

Available online 8 October 2020

Keywords:

Ultra-high energy cosmic rays

Sources

Magnetic fields

Neural networks

ABSTRACT

We present a new approach for the identification of ultra-high energy cosmic rays from sources using dynamic graph convolutional neural networks. These networks are designed to handle sparsely arranged objects and to exploit their short- and long-range correlations. Our method searches for patterns in the arrival directions of cosmic rays, which are expected to result from coherent deflections in cosmic magnetic fields. The network discriminates astrophysical scenarios with source signatures from those with only isotropically distributed cosmic rays and allows for the identification of cosmic rays that belong to a deflection pattern. We use simulated astrophysical scenarios where the source density is the only free parameter to show how density limits can be derived. We apply this method to a public data set from the AGASA Observatory.

© 2020 The Authors. Published by Elsevier B.V.

This is an open access article under the CC BY-NC-ND license (<http://creativecommons.org/licenses/by-nc-nd/4.0/>)

1. Introduction

The quest for sources of ultra-high energy cosmic rays has entered a new phase. On the one hand, the experimental results of recent years have sharpened the boundary conditions for this search; on the other hand, current developments in data analysis technologies are opening up new perspectives.

The measurements relevant to source searches include first the sharp drop in the energy spectrum above 50 EeV [1–4]. Second, measurements of the slant depth of air showers in the atmosphere indicate a mixed composition of protons and heavier nuclei [5–7]. Both these observations increase the probability of astrophysical scenarios in which the sources are some megaparsecs away and accelerate nuclei to a maximum rigidity (=energy/charge) [8]. The third relevant observation is the discovery of a large-scale dipole signal above 8 EeV energy which shows - with a significance of more than five standard deviations - that the arrival directions of cosmic rays are not entirely isotropic [9,10]. Also, there is an indication of an intermediate-scale anisotropy: the correlation of particles with energies above 39 EeV with starburst galaxies exhibits an increasing significance, currently at the 4.5σ level [11,12].

For nuclei with charge Z , deflections in cosmic magnetic fields of several degrees per charge unit are estimated [13–20], with

the strongest deflection expected in the magnetic field of our Galaxy [21–25]. The different rigidities of the nuclei may lead to patterns in the arrival directions which can be used to distinguish cosmic rays of a single source or of a concatenated source cluster from isotropically arriving particles [26,27].

In the field of data analysis, new technologies around machine learning are the driving force for much of the progress. Deep-learning methods [28] in particular have gained considerable attention in astroparticle physics [29–39].

Recently, we introduced a fit method which contracts patterns in the arrival directions induced by the Galactic magnetic field to determine most probable extragalactic source directions [40]. In this fit, several thousand parameters are determined simultaneously (source directions, particle charges), which was realized by using the backpropagation method developed for neural network training [41].

In this paper we present a new method for source identification that directly uses pattern recognition in cosmic-ray arrival directions. A similar approach using convolutional neural networks was developed in parallel [39]. Here, we use the concept of so-called dynamic graph convolutional neural networks [42] which have already been successfully adapted and applied to challenges in particle physics [43,44]. In contrast to our fit method [40], here we do not use an explicit model of the Galactic magnetic field, but instead train the network with typical deflection patterns resulting from these field models [45–50].

* Corresponding author.

E-mail address: erdmann@physik.rwth-aachen.de (M. Erdmann).

The scope of our method is to search for the existence of patterns in cosmic-ray arrival directions: if such patterns are detected by the network, we classify which individual particles originate from a common source and which can be attributed to isotropic arrival directions. For this classification we analyze variables autonomously formed by the network.

If no pattern is found, we derive a lower limit on the density of cosmic-ray sources using astrophysical simulations with the source density as their only free parameter. We exploit public data of the AGASA Observatory to demonstrate the application to real cosmic-ray measurements.

This work is structured as follows. First, we present astrophysical benchmark simulations used for training and performance estimation as well as the public dataset of the AGASA Observatory. We then introduce the functionality of dynamic graph convolutional neural networks. We describe the search for the existence of anisotropic patterns, the subsequent identification of cosmic rays and the determination of source density limits. Finally, we apply our methods to the data measured by the AGASA Observatory. We complete the work with our conclusions.

2. Cosmic rays: simulations and measurements

In this section we first present the simulated data we use for training the network and evaluating its performance.

For an in-depth understanding of the network, we start with simplified simulations in which a single source generates a few cosmic rays that exhibit expected signal patterns in the arrival directions due to the deflection in cosmic magnetic fields. As background we further add isotropically distributed cosmic rays.

Later, in an advanced simulation, we use an astrophysical scenario that depends only on one free parameter, the density of sources. Here, all cosmic rays originate from these sources, with only a few closer sources contributing several cosmic rays which form a pattern in the arrival distributions. This results in a few signal patterns distributed across the whole sky, each with particles from a common source, while most particles appear to have isotropic arrival directions.

Finally, we present the AGASA Observatory and its public data set of ultra-high energy cosmic rays.

2.1. Benchmark 1: simplified cosmic-ray simulation with a single source

In order to keep the results unambiguous and clean, this first simulation setup is simplified yet fairly in agreement with the measurements described in Section 1.

During the training process we generate up to 300.000 simulation sets on-the-fly with the following general setup. The predominant part of all N_{CRS} events, called background, is positioned isotropically on the sky. We then add a certain fraction $f_S = N_S/N_{\text{CRS}}$ of N_S signal cosmic rays which mimic a pattern arising from deflections in the Galactic magnetic field (GMF) from a source randomly located in the sky. Current models of the GMF consist of a superposition of a *coherent* field part which deflects particles in an ordered manner and a *turbulent* field part which results in blurring and widening of the incoming particle beam. The magnitude of the magnetic field influence depends on the cosmic-ray rigidity

$$R = \frac{E}{Z}, \quad (1)$$

the ratio of its energy and charge. To prevent overtraining of the network which could learn specific patterns in fixed directions of the sky we do not use one fixed field parameterization. Instead, we adopt the field magnitude of both coherent and turbulent fields from [46,48] in the following way: we account for the turbulent

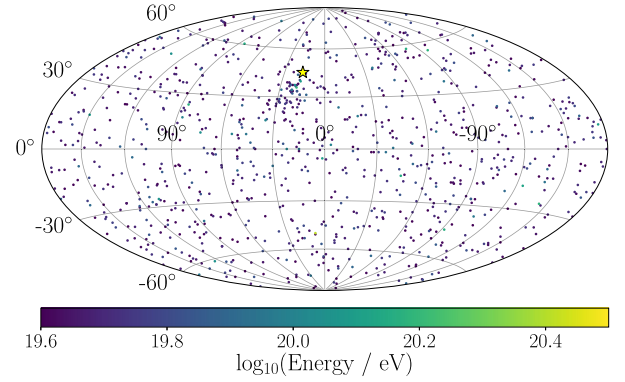


Fig. 1. Example of simulated arrival directions used for network training: the pattern induced by a magnetic field with a coherent deflection power $D = 7.2$ is situated at Galactic longitude $l \approx 16^\circ$ and Galactic latitude $b \approx 45^\circ$. The source of this signal pattern is indicated by the star symbol. It has a signal fraction of $f_S = 5.5\%$, thus $N_S = 55$ signal cosmic rays are contained in this arrival pattern. The remaining 945 events are isotropically distributed.

field by a Fisher [51] distribution with a rigidity-dependent width of

$$\sigma_{\text{turb}}(R) = \frac{T}{R / \text{EV}} \text{ rad}, \quad (2)$$

where we choose the turbulent deflection parameter T position-dependently based on typical scattering obtained in [46,48]. During the training we fix $T = 2.8$ which corresponds to half the maximum of the expected turbulent deflection in [46,48] and more than double the mean value. It was tested that training with a fixed value T for all training sets is beneficial for the network performance even when evaluating with varying values of T . Note that the effects of scattering in the extragalactic magnetic field which exhibit comparably small field amplitudes of $\mathcal{O}(10^{-15} \text{ G})$ [52], can be absorbed by the turbulent deflection parameter T as well.

The coherent deflection angle δ_{coh} is described by

$$\delta_{\text{coh}}(R) = \frac{C}{R / \text{EV}} \text{ rad}, \quad (3)$$

with a varying coherent deflection power C which is determined position-dependently based on typical deflections from [46]. For the training it is taken from a Gaussian distribution based on deflections again from [46]. Additionally, a lower cut on C ensures that the coherent deflection mostly remains larger than the turbulent one. The orientation of the signal pattern is randomly chosen to eliminate model dependencies.

The cosmic-ray energies follow the parameterized measured energy spectrum given in [53] which contains a broken power law with a smooth transition function above the ankle. The energy threshold of 40 EeV is oriented on the data used for the recent first indication of intermediate-scale anisotropy in cosmic-ray arrival directions [11]. At these high energies typical analyses of modern observatories contain around $\mathcal{O}(1000)$ events which our simulation accounts for with a total event number of $N_{\text{CRS}} = 1000$.

A pure helium composition is chosen for the network training to enable the learning of comprehensive energy orderings. Also, having a mono-atomic composition ensures that the network does not artificially learn ratios between elemental fractions which could differ between simulations and data. Nevertheless, using helium instead of protons accounts for the measured heavier component of cosmic rays at the highest energies. An example simulation is shown in Fig. 1.

To evaluate the network performance we also simulate a mixed composition scenario of the same kind using 15% hydrogen, 45% helium and 40% carbon, nitrogen and oxygen (in equal parts) nuclei.

2.2. Benchmark 2: general astrophysical simulation originating from a source population

In the previous section we introduced a simple astrophysical simulation consisting of two parts, an isotropic background and an additional magnetic-field induced arrival pattern with an arbitrarily fixed number of signal cosmic rays. In the following we extend this simplified approach to constrain actual physics quantities using the network.

A common assumption is to consider a uniformly distributed source population with source density $\rho_S = N_{\text{sources}} / V$, thus exhibiting an average number of N_{sources} source candidates in any given spatial volume V . Each of the sources accelerates nuclei of nuclear fractions f_A with a simple power-law energy spectrum of spectral index γ and maximum rigidity cut-off R_{cut} :

$$\frac{dN_A}{dE} \propto f_A \cdot E^{-\gamma} \cdot f_{\text{cut}}(E, Z_A R_{\text{cut}}). \quad (4)$$

These nuclei are emitted isotropically and they propagate through the universe before arriving on Earth. More details about the source modeling, e.g. the cut-off function f_{cut} , can be found in [8].

Under the conditions that each source i emits the same number of nuclei with the same energy spectrum and the extragalactic magnetic field is weak compared to the Galactic one, the arriving particle flux f per source above an energy threshold at the edge of our Galaxy depends on only two aspects.

The first one is the geometrical effect in a three-dimensional propagation scenario where the flux f_i of a source i at distance d_i decreases with $f_i \propto d_i^{-2}$ while the source number per distance shell increases by $N_{\text{sources}} \propto d_i^2$. Thus, the geometrical effect alone would result in a constant flux per distance bin.

The second important effect is interactions during cosmic-ray propagation, e.g. with photon fields, where particles lose energy and the composition changes. Additionally, nuclear decay and cosmological effects can attenuate particles. When combined, these processes cause a suppression of particles from faraway sources. Thus, overall this scenario will again result in some prominent sources and a practically isotropic background of farther sources of which only very few particles arrive on Earth.

The parameters describing the sources within this general universe setup have been evaluated before, using a combined fit of energy spectrum and composition of one-dimensional CR-Propa3 [54] simulations to cosmic-ray data measured by the Pierre Auger Observatory [8]. In summary, the determined source parameters were: a spectral index of $\gamma = 0.87$, a rigidity cut-off at $\log_{10}(R_{\text{cut}}/V) = 18.62$, and a composition containing 88 percent nitrogen and 12 percent silicon (for details see [8]). When arriving on Earth, the composition was altered due to propagation effects.

We now combine these one-dimensional propagation results with the described three-dimensional simulation setup including both geometrical and interaction effects. The only free parameter is the source density ρ_S which regulates the number and strength of the patterns induced by nearby sources. For a small source density there are only few and therefore very prominent nearby sources; this results in rather obvious anisotropic arrival patterns within an isotropic background. For high source densities we therefore expect predominantly isotropic arrival directions.

Having these extragalactic arrival directions we can treat deflections by the GMF analogously as in Section 2.1. Therefore, the magnitude of the coherent and of the turbulent deflection respectively again follow [46,48]. Different to the first simulation this time cosmic rays originate from more than one source and thus a related deflection model has to be applied on the sphere as a whole. This is ensured by using a HEALPix map [55,56] of the direction of the coherent deflection in [46,48].

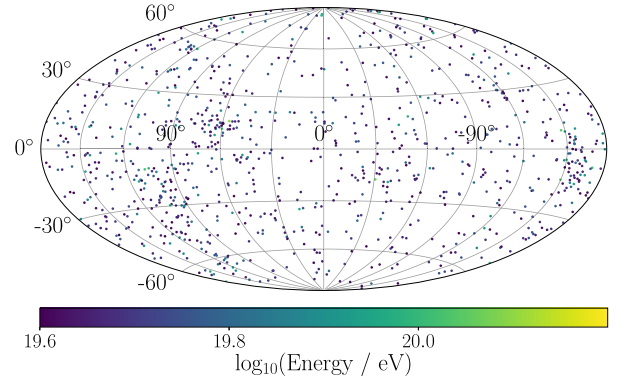


Fig. 2. Example of simulated arrival directions at a source density of $10^{-3}/\text{Mpc}^3$. For this rather small source density an anisotropic distribution of cosmic rays is obvious. Note that the energy spectrum and composition of arriving cosmic rays is in accordance with measurements [8].

During training, $\sigma_{\text{turb}}(R)$ is again chosen independently of the cosmic-ray direction as described in Eq. (2) keeping T fixed. Additionally, a random individual rotation is applied to the direction and coherent deflection maps, resulting in different deflections in every generated sample. An example arrival directions distribution is shown in Fig. 2.

2.3. Dataset of the AGASA observatory

The Akeno Giant Air Shower Array (AGASA) consisted of 111 surface detectors deployed over an area of about 100 km² and additionally 27 muon detectors. AGASA was situated at 138° 30' E and 35° 47' N. This location determines the shape of the exposure of the observatory which we calculate according to [57]. The observatory was put into operation in 1990 [58,59] and was dismantled in 2007 [60].

The public event list for cosmic rays with energies above $E = 40$ EeV and zenith angles up to $\theta = 45^\circ$ contains 57 events in total [61,62].

3. Graph convolutional neural networks

In the following we will first present an overview of the deep learning techniques necessary for this analysis and then show the architecture of the dynamic graph convolutional neural network used.

3.1. Convolutional neural networks

Traditional convolutional neural networks [63] are most successful e.g. in computer vision and pattern recognition. The dense, discrete and regular collection of image pixels allows for scanning the image with pixelated filters of a constant extent. Usually, K filters (kernels), covering only k_n neighboring pixels, i.e. a small part of the overall image, are used. The convolution of a single filter with index a applied to pixel i of a single channel image reads:

$$f_i^a = \sum_{j=1}^{k_n} \theta_j^a x_{ij} \quad (5)$$

where θ_j^a and x_{ij} denote the trainable weights and the layer inputs, respectively. The results f_i^a are stored in a *feature map*, which in turn is scanned by further filters after adding a bias and applying an activation function. In addition to Cartesian grids, spherical grids have also been used in convolutional networks [39,64] based on the HEALPix pixelization [56].

Usually, filters for deeper layers receive information from more distant pixels due to the increasing receptive field of view, so that in a figurative sense short-range correlations can be examined in the first layers and long-range correlations in the deeper layers. All K filters indexed a with their respective parameters are trained on the basis of a task formulated in the objective function.

3.2. Graph convolutional networks

Problems for the application of standard CNNs for cosmic-ray arrival directions arise from the event-based data structure together with the sparseness at the highest energies. If one wants to position events artificially on a grid corresponding to the experimental directional resolution, the pixel occupancy is extremely sparse on the one hand and, on the other hand, in a few pixels several particles may be found which requires an algorithm to aggregate the information. Both aspects are rather unfavorable for the actual application as it leads to loss of information or major computational costs. Furthermore, most convolution algorithms are designed for Euclidean manifolds and therefore cannot handle the symmetry of spherical data.

The concept of *graph convolutional networks* (GCN) [65,66] solves the unnatural requirement of particles placed on a regular grid. In GCNs, each particle can be treated individually with its arrival direction. All particles together form a point cloud and, when using a specific neighborhood assignment, a graph. Here, the exact alignment and position of the particles has to be considered in the convolutional operation and in the structure of the graph. In this astroparticle-physics application, the graph is constructed in a spherical shape as the cosmic rays arrive almost uniformly from all directions onto Earth. The particles in immediate proximity to each other in the coordinate space are then regarded as the environment for a convolution. In contrast to standard convolutional networks, the explicit cosmic ray can still be identified in the deeper network layer allowing for node classification and high interpretability.

3.3. Dynamic graph convolutional neural networks

The special feature of *dynamic graph convolutional neural networks* (DGCNNs) is that in each layer the original graph is projected onto another graph with arbitrary dimension in coordinate space as illustrated in Fig. 3. Each particle can still be followed through the network, however, its nearest neighbors have changed. The high-dimensional coordinates which for each transition define the nearest neighbors and thus the graph are derived from the properties (features) \vec{x}_c of the particles, e.g. arrival direction, energy, shower depth, etc.

For the convolution using the kernel, the k_n nearest neighbors of a particle i are considered. Particle i has M -dimensional properties $\vec{x}_{i,c}$ which will be related to the properties of the k_n neighboring particles. The convolutional operation is implemented following [42] using a neural network which depends on all values of $\vec{x}_{i,c}$, and the differences $\vec{x}_{i,c} - \vec{x}_{j,c}$ between the M properties of the particle i and those of its neighbor j :

$$h_{\Theta}(\vec{x}_{i,c}, \vec{x}_{j,c}) = \text{NN}_{\Theta}(\vec{x}_{i,c}, \vec{x}_{i,c} - \vec{x}_{j,c}), \quad (6)$$

where Θ are trainable parameters of the kernel network NN_{Θ} . The same kernel network is then applied to all k_n neighbors. The final result of the convolution for particle i can be obtained by an aggregation over the neighborhood, e.g. by calculating the average value:

$$\vec{x}'_{i,c} = \frac{1}{k_n} \sum_{j=1}^{k_n} h_{\Theta}(\vec{x}_{i,c}, \vec{x}_{j,c}). \quad (7)$$

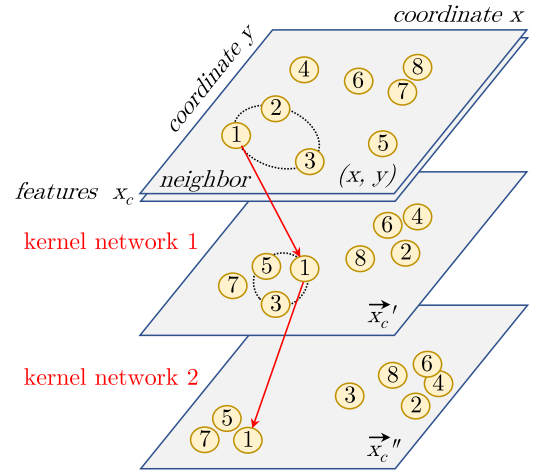


Fig. 3. Principle of a dynamic graph convolutional neural network with the example of 8 cosmic rays with arrival coordinates (x, y) and properties \vec{x}_c (features). The convolution operation is performed by a neural network on the coordinates and features, using the 2 nearest neighbors of each particle. The result of the operation is placed in a new high-dimensional space, thereby changing the neighborhood of the cosmic rays. In this way, the arrival patterns of the cosmic rays, even if they are distributed over the entire sphere, can be jointly characterized immediately in the following network layer.

The output dimension of the kernel network then defines the new dimension of the coordinate space for the resulting new graph consisting of the N_{CRs} cosmic rays, illustrated in Fig. 3. The original N -dimensional coordinate space (x, y) is extended, resulting in a new graph of K feature dimensions, denoted by \vec{x}'_c in the middle plane of Fig. 3. This is the decisive difference to a classic graph convolutional network: the clustered particles are not necessarily next to each other in their original spatial coordinates. Thus, new neighborhoods resulting from the similar properties of the particles are investigated in the forthcoming convolutional layer.

Also, the following convolutional layer is realized by a network (cf. Fig. 3 lower level). As the rearranged particles inherit new neighbors, both short- and long-range correlations are already analyzed at this step. If a binary classifier is trained using the objective function, the parameters of the two neighboring networks will be adjusted such that two separate groups of particles become visible in the high-dimensional space denoted by \vec{x}''_c in the figure.

3.4. Network architecture

Our implementation¹ of the network architecture is inspired by [43]. In this reference, Eq. (7) is referred to as *EdgeConv* layer [42]. In Fig. 4, we show at the top the input with the N -dimensional coordinate space and the M -dimensional feature space.

Instead of expressing the cosmic-ray arrival direction by spherical coordinates (θ, ϕ) , we use the three-dimensional normalized vector (x, y, z) of the arrival direction to avoid discontinuities in spherical coordinates. As input features we use the arrival direction together with the energy of the cosmic ray, thus four dimensions (x, y, z, E) .

While the normalized directional vector (x, y, z) has reasonable numerical values by definition, the strong variation in the values of the cosmic-ray energies is reduced prior to the network input. By using a transformation of the energy $E' = (56 \text{ EeV}/E)^3$ the energy distribution becomes more uniform with most values at $\mathcal{O}(1)$.

As the neighborhood we consider the $k_n = 16$ nearest particles in coordinate space or in the combined coordinate and feature

¹ code available at https://git.rwth-aachen.de/niklas.langner/edgeconv_keras

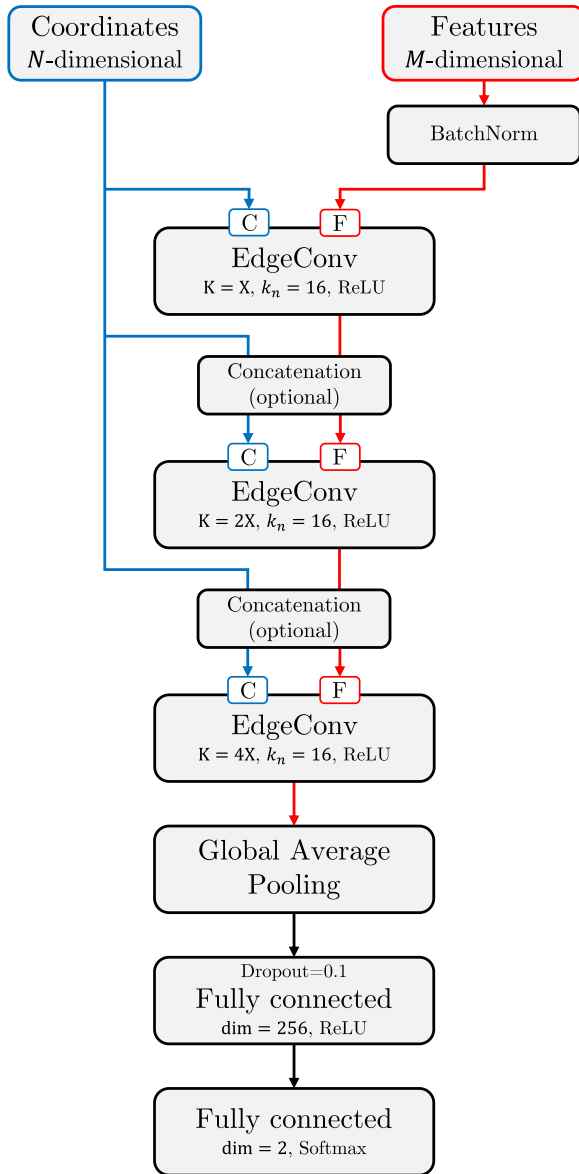


Fig. 4. Architecture of the applied neural network. The $k_n = 16$ nearest neighbors of each particle are determined from the coordinate space C. The convolutional operations on the features F are performed three times in EdgeConv blocks. Optionally, neighbored particles are fixed through all calculations of the network or varied by concatenation of the spatial coordinates with the features obtained with the convolutional operations.

space, respectively. When varying this number we found no improvement for the tasks studied in this work.

In the first EdgeConv layer, the k_n nearest neighbors are calculated using the initial coordinates of the cosmic rays (input C in Fig. 4). The convolutions are applied to their features (input F in Fig. 4). Each EdgeConv layer performs one convolution as described in Eq. (7) using a kernel network with three fully connected layers of the same dimension K. Batch normalization with momentum of 0.9 and $\epsilon = 10^{-5}$ as well as ReLU activation are applied after each layer. Finally, the average over all neighbors is taken to obtain a permutational invariant layer. The dimension K of the convolution kernels is adjusted according to the specific task studied below. These successive transformations can be understood as a continuous and non-linear filter applied to each cosmic-ray neighborhood.

We use this network either as a graph convolutional neural network (GCN) by limiting the coordinates given to all subsequent

EdgeConv layers to the cosmic-ray arrival directions, or alternatively as a dynamic graph convolutional neural network (DGCNN) by extending the coordinates with the feature space obtained in the previous EdgeConv layer. Only in the latter case do we allow new neighborhoods to be formed. Depending on the task to be solved, we find advantages for either of the network architectures.

After the convolutions, global average pooling is used to gather the global information contained in all cosmic rays. Using two fully-connected layers and a final softmax activation, a binary output is achieved which we call:

$$\text{signal} : x_{\text{sig}} \quad \text{isotropy} : (1 - x_{\text{sig}}) \quad (8)$$

Thus, this final output of the network can be interpreted as a probability x_{sig} that the corresponding set of cosmic rays contains an arrival pattern which originated from a source.

4. Searching for cosmic-ray sources

We evaluate the performance of the network in three challenges. In the first challenge, the goal is to recognize whether a signal pattern of a source is present within the arrival directions and energies of 1000 cosmic rays according to the benchmark 1 simulation from Section 2.1. In an extension, the second challenge is to classify each particle as either belonging to a source or to an isotropic contribution. In the third task, the network should recognize whether there are signal patterns of several sources distributed across the sphere as simulated with the benchmark 2 setup from Section 2.2.

4.1. Expected sensitivity for the signal pattern of a single source

In the first task we use the GCN (Fig. 4) with the arrival directions of the cosmic rays as fixed coordinates in all convolutional layers. This is meaningful as there is at most one coherent signal pattern on the sphere of arrival directions. An experiment with the DGCNN exhibited no improvement because there was no need to merge signal patterns scattered across the sphere.

We use $K = 16$ convolution kernels in the first EdgeConv layer and increase this number in the following layers as shown in Fig. 4. After the global average pooling, a fully-connected layer with 256 nodes is used. These hyperparameters were optimized by a scan. The categorical cross entropy was used as the objective function, and the Adam optimizer [67] was used for training. The learning rate was scheduled to drop from 10^{-3} to 10^{-5} during the first two thirds of the training, following the falling range of the cosine function (between 0 and π). The batch size was set to 60 using 30 sets of 1000 arrival directions with a signal pattern of 55 helium nuclei from a source and 30 sets of 1000 isotropically distributed arrival directions. The comparatively high signal fraction during training proved to be advantageous, since the fully trained network is then able to detect anisotropic arrival patterns even with much smaller signal fractions. Training experiments on different signal fractions or with a mixed composition provided no improvement.

The expected sensitivity of the network prediction was evaluated on 1000 signal sets each with a total of 1000 cosmic rays, of which a varying number N_s originate from a source and 10^7 sets with isotropic arrival directions (cf. Section 2.1). We show both the evaluation with helium nuclei and the evaluation with a mixed composition. Keep in mind that, in both cases, the network is trained with helium nuclei only.

The final value x_{sig} of the softmax function for each of the signal sets was compared to the values of the isotropic sets. We define the p-value as the relative number of isotropic sets whose function value x_{sig} exceeds that of the signal set.

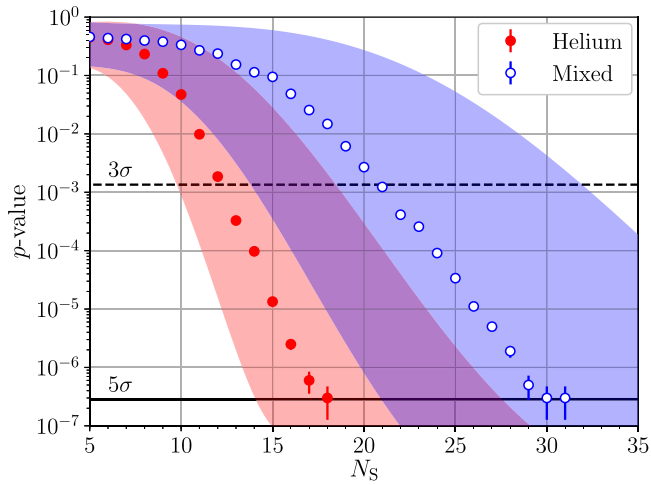


Fig. 5. Isotropic chance probability to reach a network response at least as high as a signal enriched simulation as a function of the number N_s of source cosmic rays according to the benchmark 1 simulation. The total number of events in one simulated dataset is 1000. Shown is the median p -value from 1000 simulated evaluations for a helium composition (solid red symbols) and for a mixed composition (open blue symbols). Transparent bands represent the 68% quantile. The network was trained on signal scenarios with $N_s = 55$ source nuclei and scenarios of solely isotropic arrival directions, both containing helium nuclei only. (For interpretation of the references to colour in this figure legend, the reader is referred to the web version of this article.)

In Fig. 5 we show the median of these p -values for all 1000 signal sets as a function of the number of simulated cosmic rays belonging to the signal pattern. As expected, the mono-atomic case is easier as all cosmic rays of a pattern are ordered according to their energy and the charges have no additional influence on the deflection angle. Here, for 13 source nuclei in 1000 cosmic rays a signal pattern is detected with more than 3σ (standard deviations). The threshold of 5σ is reached with 19 helium nuclei from one source. For comparison, the p -values using two-point autocorrelation with 180 angle bins are calculated by individually choosing the bin with the lowest p -value for each simulation. With median sensitivities of 2.7σ and 4.4σ for 13 and 19 source nuclei respectively, the two-point autocorrelation does not reach the graph network's sensitivity even without penalizing the scan over 180 angle bins.

Using the network with a mixed composition, the minimum number of particles from one source increases to 21 (3σ) or 32 (5σ), respectively. These numbers are remarkable considering that the network never actually dealt with mixed charges during training. If the network were to exploit only the helium nuclei that it was trained on with a contribution of 45% to the mixed-composition scenario, one would expect that 42 cosmic rays would be needed for an effect of 5 standard deviations. Thus, to achieve the same effect with fewer cosmic rays, the network also exploits information carried by the other nuclei.

4.2. Identification of cosmic rays from a source

In the second task, each individual cosmic ray will be examined to establish whether it belongs to a signal pattern and thus originates from a common source, or whether it is a particle of the isotropic arrival distribution.

For this classification we analyze the autonomously formed variables of the network before the pooling layer as described in the following. Changing the network's output layer to perform a binary classification of each of the 1000 cosmic rays yielded only slightly better results. For the benefit of an insight into the functioning of the original network, however, here we decide for cosmic-ray identification using this approach.

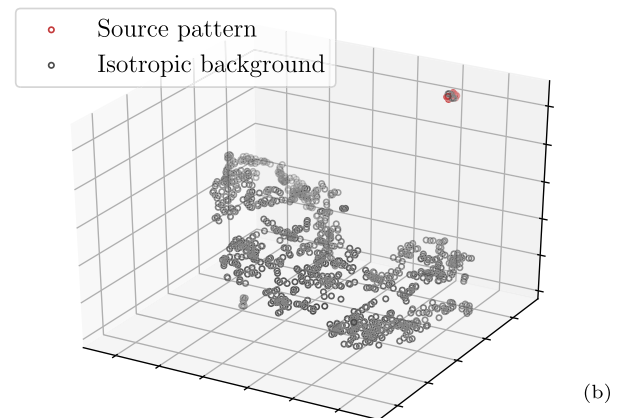
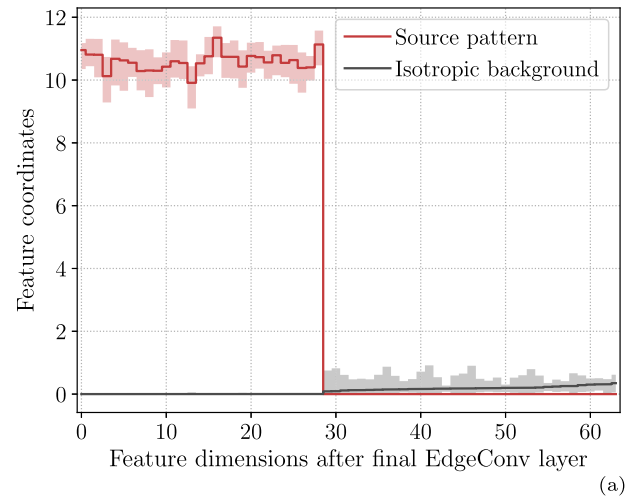


Fig. 6. Visualization of the network for separating signal cosmic rays (red) from isotropic cosmic rays (gray) in the benchmark 1 simulation. For a single simulated data set with 1000 cosmic rays, 15 of which originate from a common source the median values seen in (a) (solid lines) are calculated for each of the 64 dimensions of the final EdgeConv layer. The shaded areas represent the 68% quantile. (b) A three-dimensional representation of the final EdgeConv layer's output is created using the t-SNE technique [68]. (For interpretation of the references to colour in this figure legend, the reader is referred to the web version of this article.)

After the final EdgeConv layer with 64 kernels ($K = 4 \times 16$, cf. Fig. 4), each cosmic ray is represented as a vector in a 64-dimensional feature space resulting in a total dimensionality of ($64 \times N_{CRs}$). The pooling layer takes the mean over all cosmic rays resulting in 64 output values. These encode the information about whether or not there is a signal pattern in the arrival directions of the cosmic rays, which is then processed by the subsequent fully connected layers to provide the final binary output. Instead, we now use the complete information of ($64 \times N_{CRs}$) values before the pooling layer to identify cosmic rays originating from the source or from the isotropic arrival distribution.

In Fig. 6a we show the median values for each of the 64 dimensions for a single set of 1000 cosmic rays. The 15 cosmic rays from the source are denoted by the dark-red marked distribution and the median values of isotropically arriving particles are shown as a distribution marked in gray. The order of the 64 variables is arbitrary and shown here for visualization purposes in a way that the median value for the isotropic distribution increases. The colored areas around the median values denote the 68% quantile of the values of all contributing cosmic rays.

For the particles from isotropic arrival distributions the median values are close to zero in all dimensions, and even invisible in the

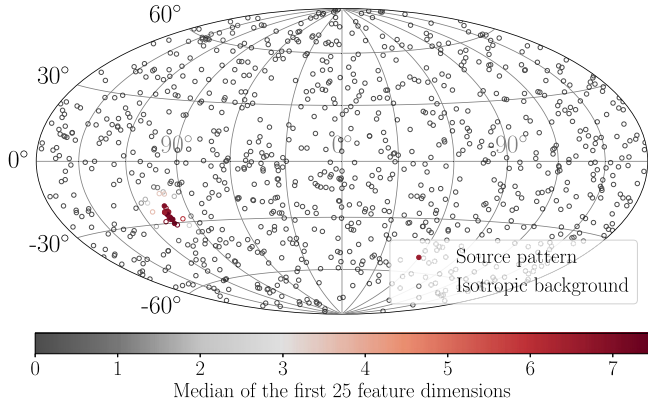


Fig. 7. Classified arrival directions in benchmark 1 simulation: the color scale indicates the median of the first 25 feature dimensions. A cosmic ray is identified as signal with a median of the 25 feature values greater than 3 and is otherwise attributed to isotropy. The signal pattern (denoted by filled circles) is correctly identified. (For interpretation of the references to colour in this figure legend, the reader is referred to the web version of this article.)

figure for dimensions 0 to 28 owing to their small values. For the particles of a signal pattern the information appears to be encoded in the dimensions 0 to 28 with median values around 11. In the last 35 dimensions, however, the median values of signal cosmic rays are close to zero. Thus, the network allocates approximately half of the available feature dimensions for cosmic rays originating from the source, while the other half is used for isotropic cosmic rays. This indicates that the network effectively performs clustering in the high-dimensional feature space which separates the signal cosmic rays from the isotropic ones.

For an additional visualization of this process we use the t-SNE algorithm. This algorithm embeds high-dimensional data in a reduced number of dimensions by keeping the implicit structure, i.e. neighborhoods and connections, in place. For further information refer to [68].

The three-dimensional representation of the 64-dimensional point cloud after the final EdgeConv layer is shown in Fig. 6b. One can see clear clustering of the cosmic rays from the source pattern, while some isotropic cosmic rays are also clustered near this region.

To distinguish between cosmic rays that most likely originated in a source and isotropic ones we make use of the network's clustering of source cosmic rays in the first dimensions of the feature space. Subsequently, for each cosmic ray we take the median of the first 25 dimensions (preserving a buffer zone) of its vector in the feature space. We identify cosmic rays with a median value greater than 3 as coming from a source and below 3 as belonging to the isotropically arriving distribution. We have verified that this threshold works well even if the total number of cosmic rays varies.

To assess the quality of the identification, we calculate the efficiency of assigning a signal particle as belonging to the signal pattern by:

$$\epsilon = \frac{\text{\#correctly identified signal cosmic rays}}{\text{\#signal cosmic rays}} \quad (9)$$

We also calculate the purity with which a particle identified as signal actually belongs to the signal pattern of a source as:

$$\rho = \frac{\text{\#correctly identified signal cosmic rays}}{\text{\#identified signal cosmic rays}} \quad (10)$$

An example of classified arrival directions for a pure helium simulation is shown in Fig. 7. The simulated underlying signal pattern containing 15 particles is identified and all signal particles

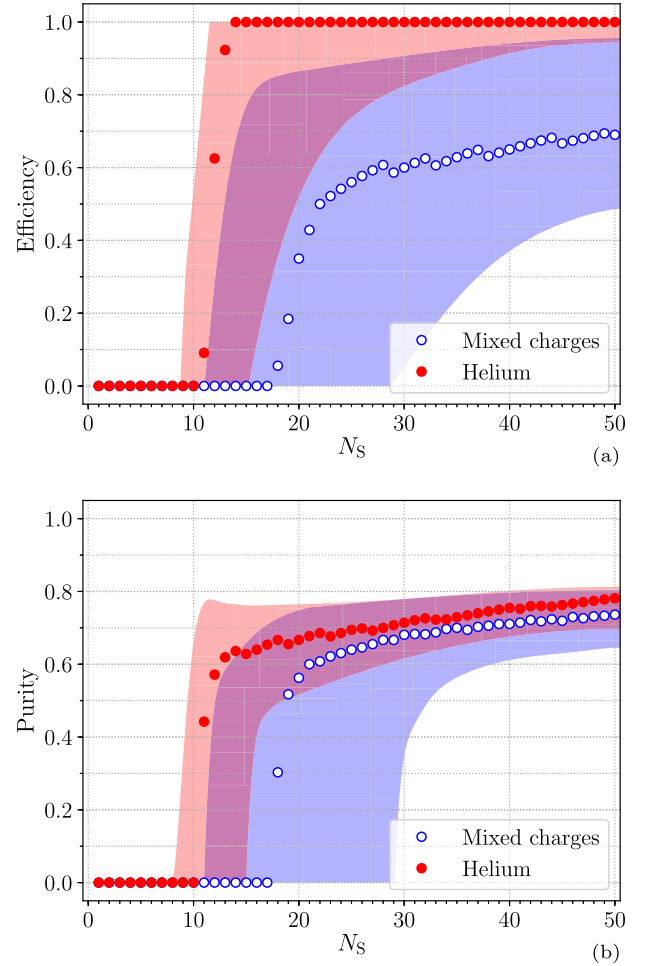


Fig. 8. Median efficiency (a) and purity (b) of 500 simulated sets as a function of the number of signal cosmic rays N_s coming from a single source in the benchmark 1 simulation. Both the pure helium (solid red) and the mixed composition (blue) are shown. Transparent bands represent the 68% quantile. (For interpretation of the references to colour in this figure legend, the reader is referred to the web version of this article.)

were labeled correctly with an efficiency of 100%. Some surrounding isotropic particles were incorrectly classified in this example with a median greater than 3, which reduces the purity to 65.2%.

To assess whether or not this is a representative example we examine 500 sets with varying numbers of signal cosmic rays. In Fig. 8 we show the efficiency and purity as a function of the number of signal particles of a source separately for the scenario with pure helium and for the mixed composition.

For the helium scenario, 19 signal particles from one source were required to achieve a significance of 5 standard deviations (cf. Fig. 5). If the pattern is detected, in median all 19 cosmic rays are identified correctly with an efficiency of 100 percent as shown in Fig. 8a. Nevertheless there are cases where fewer or even no cosmic rays with median feature dimension values above 3 are detected resulting in cases with a low efficiency. This is shown by the shaded region representing the 68% interval in Fig. 8a. The median purity of 65% shown in Fig. 8b is still rather low at $N_s = 19$ and exhibits a large spread. This means that, in addition to the (in median) 19 correctly identified source particles, (in median) 10 of the isotropically arriving particles are incorrectly identified as signals. In the mixed composition case, 32 identified source particles for 5 standard deviations have an efficiency and purity of around 60% – 70%.

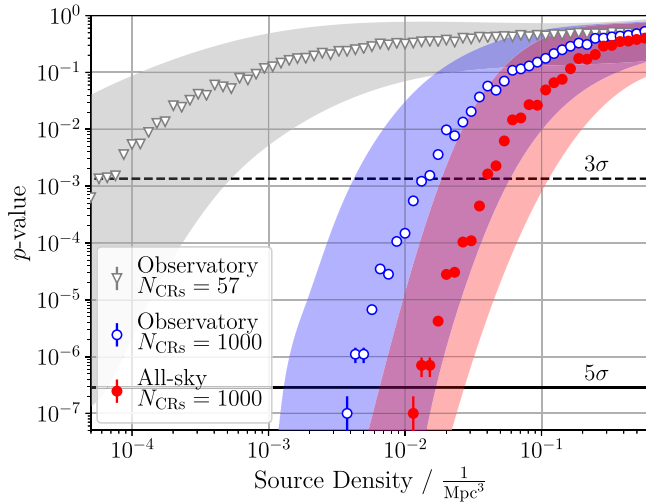


Fig. 9. Probability of the cosmic-ray arrival directions with multiple signal patterns to originate from isotropic scenarios as a function of the source density. The signal patterns were simulated using the general astrophysical benchmark 2 scenario (cf. Section 2.2). The median p -values from 1000 simulations are represented by symbols and transparent bands represent the 68% quantile. (For interpretation of the references to colour in this figure legend, the reader is referred to the web version of this article.)

4.3. Search for multiple cosmic-ray sources

In the third challenge, we again aim to identify signal patterns in the arrival directions and energies of cosmic rays. Due to the general astrophysical benchmark 2 scenario used (cf. Section 2.2), there may be signal patterns from several different sources, each contributing different numbers of cosmic rays.

For this analysis we use the dynamic graph convolutional network (DGCNN) with the extension of the coordinate space from the second network layer onward by considering the arrival directions of the particles as well as the features resulting from both the particles and their neighborhoods. Thus, the network has the possibility to change neighborhoods in deeper layers in such a way that neighborhood properties can be exploited for the respective challenge. Here, we find that the dynamic graph network performs better than the graph network with fixed neighborhoods. Since signal patterns can appear anywhere on the arrival sphere of the particles, the dynamic graph network can effectively analyze the signal patterns of different localizations on the sphere at an early stage by forming suitable neighborhoods. Optimized by scanning we decide to increase the kernel size from $K = 64$ in the first EdgeConv layer to $K = 256$ in the last one.

As training data we use simulated astrophysical scenarios with a source density of 10^{-3} Mpc^{-3} . At this rather small source density the arrival directions exhibit stronger anisotropies (cf. Fig. 2) which enables a stable training process. It was verified in a scan over the source density that 10^{-3} Mpc^{-3} is a reasonable choice.

As isotropic comparison we also use the same scenarios, but randomize the arrival directions. In this way we ensure that the energy distribution of the cosmic rays remains unchanged.

We follow the previously outlined calculation of the p -value: first, we calculate the network prediction x_{sig} of 1000 simulated scenarios with signal patterns from different sources. We then determine the relative number of isotropic scenarios that have a larger value x_{sig} than each of the signal scenarios.

In Fig. 9 we show the median p -value, determined from the 1000 signal scenarios, as a function of the source density. Under the conditions of this general astrophysical scenario, a set of 1000 arriving cosmic rays with signal patterns can be identified with

3 standard deviations at a source density of $4.0 \cdot 10^{-2} \text{ Mpc}^{-3}$. The limit of 5 standard deviations is reached at a source density of $1.2 \cdot 10^{-2} \text{ Mpc}^{-3}$.

If data of an observatory which can observe only a part of the sphere are used, the sensitivity decreases accordingly. Here, we use the geometric exposure of the AGASA Observatory by way of example while keeping N_{CRs} at 1000. The blue symbols in Fig. 9 denote the corresponding reduced exclusion limits where the 5σ confidence limit is reached for $4 \cdot 10^{-3} \text{ Mpc}^{-3}$.

Additionally, we explore the sensitivity of the network on a dataset with only $N_{\text{CRs}} = 57$ cosmic rays following the AGASA exposure. The corresponding p -values are shown in gray in Fig. 9. One can see that the sensitivity is considerably reduced as expected. The 3σ confidence limit is only reached for a source density of $6 \cdot 10^{-5} \text{ Mpc}^{-3}$ and the 5σ at $4 \cdot 10^{-6} \text{ Mpc}^{-3}$.

5. Source density limit from AGASA data

In this section we apply the dynamic graph convolutional network to the 57 ultra-high energy events of the AGASA Observatory (cf. Section 2.3). To begin with, we train the network using simulated datasets with 57 cosmic rays within the exposure of the observatory. For the training we use the generalized astrophysical scenario (cf. Section 2.2) with source density as the only free parameter where we determined $\rho_s = 10^{-4} \text{ Mpc}^{-3}$ to be a good choice based on a scan on simulations. To account for the difference between the energy spectrum of the AGASA data and the simulated one, we replace the cosmic-ray energies before applying the deflection in the simulation: for this, 57 random energies are sampled from a power law spectrum with $\gamma = -3.4$, which results in a median energy close to the median of the AGASA measurements. The energies are replaced such that the order of the energy values remains the same.

For the measured 57 events, we determine the p -value as presented in Section 4.1. For that, we generate isotropic sets of 57 cosmic rays by randomizing the arrival directions of the measured events. This procedure again ensures that the energy distribution of the cosmic rays remains unchanged.

The network response x_{sig} on the AGASA dataset lies fairly within the isotropic expectation and is exceeded by $p = 82\%$ of the isotropic simulations. Thus, in the relatively few events of the AGASA Observatory the network finds no signs of signal patterns in the arrival directions. Therefore, we calculate a lower limit for the source density for the generalized astrophysical scenario. To this end, we invert the question and ask what minimum source density ρ_s the generalized astrophysical scenario needs to have in order to satisfy the p -value of the data. For this purpose, we investigate the distribution of the p -values for 1000 simulated data sets at each source density ρ_s of the generalized astrophysical scenario.

Assuming that the regular and turbulent components of the intervening magnetic field are of the correct order of magnitude, we can state a lower limit of $2 \cdot 10^{-3} \text{ Mpc}^{-3}$ for the density of cosmic-ray sources at 95% confidence level in the context of this astrophysical scenario.

This limit is an order of magnitude larger than values obtained comparing the measured two-point autocorrelation of the data of the Pierre Auger Observatory with simulations [69,70]. It should be noted though, that all source density limits depend not only on the analysis method, but also on the simulated astrophysical scenario. Unique properties of the scenarios used in our limit calculation are mixed nuclear composition and coherent magnetic field deflections.

According to Fig. 9, we expect that a larger number of cosmic rays, such as those measured by modern observatories, will significantly improve the determination of the source density. In addition, signal patterns could be detected by the higher data statistics.

6. Conclusion

In this work we investigated graph networks for the identification of source patterns in the cosmic-ray arrival directions and energies. These source patterns originate from cosmic nuclei that are deflected in the coherent magnetic field of our Galaxy and allow cosmic-ray sources to be identified.

Graph convolutional networks are particularly well suited to investigate cosmic rays with their individual arrival directions without digitizing the directions on a Cartesian or spherical grid. The convolutional operation is defined by the particles' nearest neighbors, whose properties are characterized in a K -dimensional space.

When classifying a data set as either isotropic background or containing a signal pattern, our investigations show that the particles of a signal pattern are bundled in the K -dimensional property space separately from the isotropically arriving particles.

The network thus identifies data sets with a signal pattern of 19 helium nuclei in 981 isotropically distributed particles with a confidence of 5 standard deviations against isotropic data sets. Additionally, in median the network correctly identifies all 19 helium nuclei from the signal pattern and incorrectly identifies 10 particles that actually belong to the isotropic background.

For a generalized astrophysical scenario, which depends only on the source density and generates multiple source patterns distributed over the sphere, dynamic graph convolutional networks prove to be advantageous. In this case, the neighborhoods of the particles in deeper network layers can be optimized for the convolutional operation in such a way that the properties of signal patterns can be studied together despite very different spatial arrival directions.

As a measure for the sensitivity of such networks, we expect that the existence of signal patterns can be proven with 5 standard deviations for 1000 cosmic rays at an upper limit for the source density of $1.5 \cdot 10^{-2} \text{ Mpc}^{-3}$.

As an example for data measured by an observatory we analyzed the public data of the AGASA experiment with energies above 40 EeV. A signal pattern could not be detected here with 57 cosmic rays only. However, from these data we give a lower limit on the source density of the generalized astrophysical scenario of $\rho_s^{95} = 2 \cdot 10^{-3} \text{ Mpc}^{-3}$ at 95% confidence level assuming that the impact of magnetic fields is reasonably estimated.

We also show that we could greatly improve such an exclusion limit for the source density when using data from current observatories with more than 1000 cosmic rays. Furthermore, patterns may be found and thus sources of ultra-high energy cosmic rays identified.

Declaration of Competing Interest

The authors declare that they have no known competing financial interests or personal relationships that could have appeared to influence the work reported in this paper.

Acknowledgments

We wish to thank Yannik Rath for his valuable comments on the manuscript. This work is supported by the Ministry of Innovation, Science and Research of the State of North Rhine-Westphalia, and by the Federal Ministry of Education and Research (BMBF).

References

- [1] J. Abraham, et al., Observation of the suppression of the flux of cosmic rays above $4 \times 10^{19} \text{ eV}$, *Phys. Rev. Lett.* 101 (2008) 061101, doi:[10.1103/PhysRevLett.101.061101](https://doi.org/10.1103/PhysRevLett.101.061101).
- [2] J. Abraham, et al., Measurement of the energy spectrum of cosmic rays above 10^{18} eV using the Pierre Auger Observatory, *Phys. Lett. B* 685 (2010) 239–246, doi:[10.1016/j.physletb.2010.02.013](https://doi.org/10.1016/j.physletb.2010.02.013).
- [3] T. Abu-Zayyad, et al., The cosmic ray energy spectrum observed with the surface detector of the telescope array experiment, *Astrophys. J.* 768 (2013) L1, doi:[10.1088/2041-8205/768/1/L1](https://doi.org/10.1088/2041-8205/768/1/L1).
- [4] A. Aab, et al., Measurement of the cosmic ray spectrum above $4 \times 10^{18} \text{ eV}$ using inclined events detected with the Pierre Auger Observatory, *JCAP* 1508 (2015) 049, doi:[10.1088/1475-7516/2015/08/049](https://doi.org/10.1088/1475-7516/2015/08/049).
- [5] A. Aab, et al., Depth of maximum of air-shower profiles at the Pierre Auger Observatory: measurements at energies above $10^{17.8} \text{ eV}$, *Phys. Rev. D* 90 (12) (2014a) 122005, doi:[10.1103/PhysRevD.90.122005](https://doi.org/10.1103/PhysRevD.90.122005).
- [6] A. Aab, et al., Depth of maximum of air-shower profiles at the Pierre Auger Observatory. II. Composition implications, *Phys. Rev. D* 90 (2014b) 122006, doi:[10.1103/PhysRevD.90.122006](https://doi.org/10.1103/PhysRevD.90.122006).
- [7] A. Aab, et al., Inferences on mass composition and tests of hadronic interactions from 0.3 to 100 EeV using the water-Cherenkov detectors of the Pierre Auger Observatory, *Phys. Rev. D* 96 (12) (2017a) 122003, doi:[10.1103/PhysRevD.96.122003](https://doi.org/10.1103/PhysRevD.96.122003).
- [8] A. Aab, et al., Combined fit of spectrum and composition data as measured by the Pierre Auger Observatory, *JCAP* 1704 (04) (2017b) 038, doi:[10.1088/1475-7516/2017/04/038](https://doi.org/10.1088/1475-7516/2017/04/038), doi:[10.1088/1475-7516/2017/04/038](https://doi.org/10.1088/1475-7516/2017/04/038), [Erratum: *JCAP* 1803, no.03, E02(2018)].
- [9] A. Aab, et al., Observation of a large-scale anisotropy in the arrival directions of cosmic rays above $8 \times 10^{18} \text{ eV}$, *Science* 357 (6537) (2017c) 1266–1270, doi:[10.1126/science.1266666](https://doi.org/10.1126/science.1266666).
- [10] A. Aab, et al., Large-scale cosmic-ray anisotropies above 4 EeV measured by the Pierre Auger Observatory, *Astrophys. J.* 868 (1) (2018a) 4, doi:[10.3847/1538-4357/aac689](https://doi.org/10.3847/1538-4357/aac689).
- [11] A. Aab, et al., An Indication of anisotropy in arrival directions of ultra-high-energy cosmic rays through comparison to the flux pattern of extragalactic gamma-ray sources, *Astrophys. J.* 853 (2) (2018b) L29, doi:[10.3847/2041-8213/aaa66d](https://doi.org/10.3847/2041-8213/aaa66d).
- [12] L. Caccianiga, Anisotropies of the highest energy cosmic-ray events recorded by the Pierre Auger Observatory in 15 years of operation, *PoS ICRC2019* (2019) 206, <https://pos.sissa.it/358/206>.
- [13] T. Stanev, Ultrahigh-energy cosmic rays and the large scale structure of the galactic magnetic field, *Astrophys. J.* 479 (1997) 290, doi:[10.1086/303866](https://doi.org/10.1086/303866).
- [14] D. Harari, S. Mollerach, E. Roulet, Signatures of galactic magnetic lensing upon ultrahigh-energy cosmic rays, *JHEP* 02 (2000) 035, doi:[10.1088/1126-6708/2000/02/035](https://doi.org/10.1088/1126-6708/2000/02/035).
- [15] D. Harari, S. Mollerach, E. Roulet, F. Sanchez, Lensing of ultrahigh-energy cosmic rays in turbulent magnetic fields, *JHEP* 03 (2002) 045, doi:[10.1088/1126-6708/2002/03/045](https://doi.org/10.1088/1126-6708/2002/03/045).
- [16] G. Golup, D. Harari, S. Mollerach, E. Roulet, Source position reconstruction and constraints on the galactic magnetic field from ultra-high energy cosmic rays, *Astropart. Phys.* 32 (2009) 269–277, doi:[10.1016/j.astropartphys.2009.09.003](https://doi.org/10.1016/j.astropartphys.2009.09.003).
- [17] G. Giacinti, M. Kachelriess, D.V. Semikoz, G. Sigl, Ultrahigh energy nuclei in the galactic magnetic field, *JCAP* 1008 (2010) 036, doi:[10.1088/1475-7516/2010/08/036](https://doi.org/10.1088/1475-7516/2010/08/036).
- [18] Y.-Y. Jiang, L.G. Hou, J.L. Han, X.H. Sun, W. Wang, Do ultrahigh energy cosmic rays come from active galactic nuclei and fermi γ -ray sources? *Astrophys. J.* 719 (1) (2010) 459–468, doi:[10.1088/0004-637x/719/1/459](https://doi.org/10.1088/0004-637x/719/1/459).
- [19] G. Golup, D. Harari, S. Mollerach, E. Roulet, Searching for signals of magnetic lensing in ultra-high energy cosmic rays, *JCAP* 1107 (2011) 006, doi:[10.1088/1475-7516/2011/07/006](https://doi.org/10.1088/1475-7516/2011/07/006).
- [20] G. Giacinti, M. Kachelriess, D.V. Semikoz, G. Sigl, Ultrahigh energy nuclei in the turbulent galactic magnetic field, *Astropart. Phys.* 35 (2011) 192–200, doi:[10.1016/j.astropartphys.2011.07.006](https://doi.org/10.1016/j.astropartphys.2011.07.006).
- [21] K. Dolag, D. Grasso, V. Springel, I. Tkachev, Mapping deflections of ultrahigh energy cosmic rays in constrained simulations of extragalactic magnetic fields, *JETP Lett.* 79 (2004) 583–587, doi:[10.1134/1.1790011](https://doi.org/10.1134/1.1790011), [*Pisma Zh. Eksp. Teor. Fiz.* 79, 719(2004)].
- [22] D. Paoletti, F. Finelli, CMB constraints on a stochastic background of primordial magnetic fields, *Phys. Rev. D* 83 (2011) 123533, doi:[10.1103/PhysRevD.83.123533](https://doi.org/10.1103/PhysRevD.83.123533).
- [23] R. Durrer, A. Neronov, Cosmological magnetic fields: their generation, evolution and observation, *Astron. Astrophys. Rev.* 21 (2013) 62, doi:[10.1007/s00159-013-0062-7](https://doi.org/10.1007/s00159-013-0062-7).
- [24] S. Hackstein, F. Vazza, M. Brüggen, G. Sigl, A. Dundovic, Propagation of ultrahigh energy cosmic rays in extragalactic magnetic fields: a view from cosmological simulations, *Mon. Not. Roy. Astron. Soc.* 462 (4) (2016) 3660–3671, doi:[10.1093/mnras/stw1903](https://doi.org/10.1093/mnras/stw1903).
- [25] J.D. Bray, A.M.M. Scaife, An upper limit on the strength of the extragalactic magnetic field from ultra-high-energy cosmic-ray anisotropy, *Astrophys. J.* 861 (1) (2018) 3, doi:[10.3847/1538-4357/aac777](https://doi.org/10.3847/1538-4357/aac777).
- [26] P. Abreu, et al., Search for signatures of magnetically-induced alignment in the arrival directions measured by the Pierre Auger Observatory, *Astropart. Phys.* 35 (2012) 354–361, doi:[10.1016/j.astropartphys.2011.10.004](https://doi.org/10.1016/j.astropartphys.2011.10.004).
- [27] A. Aab, et al., Search for patterns by combining cosmic-ray energy and arrival directions at the Pierre Auger Observatory, *Eur. Phys. J. C* 75 (6) (2015) 269, doi:[10.1140/epjc/s10052-015-3471-0](https://doi.org/10.1140/epjc/s10052-015-3471-0).
- [28] I. Goodfellow, Y. Bengio, A. Courville, *Deep Learning*, The MIT Press, 2016.
- [29] M. Erdmann, J. Glombitza, D. Walz, A deep learning-based reconstruction of cosmic ray-induced air showers, *Astropart. Phys.* 97 (2018a) 46–53, doi:[10.1016/j.astropartphys.2017.10.006](https://doi.org/10.1016/j.astropartphys.2017.10.006).
- [30] M. Erdmann, L. Geiger, J. Glombitza, D. Schmidt, Generating and refining particle detector simulations using the Wasserstein distance in ad-

- versarial networks, *Comput. Softw. Big Sci.* 2 (1) (2018b) 4, doi:[10.1007/s41781-018-0008-x](https://doi.org/10.1007/s41781-018-0008-x).
- [31] I. Shilon, M. Kraus, M. Büchele, K. Egberts, T. Fischer, T.L. Holch, T. Lohse, U. Schwanke, C. Steppa, S. Funk, Application of deep learning methods to analysis of imaging atmospheric cherenkov telescopes data, *Astropart. Phys.* 105 (2019) 44–53, doi:[10.1016/j.astropartphys.2018.10.003](https://doi.org/10.1016/j.astropartphys.2018.10.003).
- [32] S. Delaquis, et al., Deep neural networks for energy and position reconstruction in EXO-200, *JINST* 13 (08) (2018) P08023, doi:[10.1088/1748-0221/13/08/P08023](https://doi.org/10.1088/1748-0221/13/08/P08023).
- [33] F. Führer, T. Charnock, A. Zilles, M. Tueros, Towards online triggering for the radio detection of air showers using deep neural networks, *EPJ Web Conf.* 216 (2019) 03004, doi:[10.1051/epjconf/201921603004](https://doi.org/10.1051/epjconf/201921603004).
- [34] A. Guillen, A. Bueno, J.M. Carceller, J.C. Martinez-Velazquez, G. Rubio, C.J. Toderó Peixoto, P. Sanchez-Lucas, Deep learning techniques applied to the physics of extensive air showers, *Astropart. Phys.* 111 (2019) 12–22, doi:[10.1016/j.astropartphys.2019.03.001](https://doi.org/10.1016/j.astropartphys.2019.03.001).
- [35] P. Bezyazeev, et al., Search for Neutrinoless Double-Beta Decay with the Complete EXO-200 Dataset, *Phys. Rev. Lett.* 123 (16) (2019) 161802, doi:[10.1103/PhysRevLett.123.161802](https://doi.org/10.1103/PhysRevLett.123.161802).
- [36] G. Anton, et al., Advanced signal reconstruction in Tunka-Rex with matched filtering and deep learning (2019) arXiv:[1906.10947](https://arxiv.org/abs/1906.10947).
- [37] M. Kronmueller, T. Glauch, Application of deep neural networks to event type classification in IceCube, *PoS ICRC2019* (2020) 937, doi:[10.22323/1.358.0937](https://doi.org/10.22323/1.358.0937).
- [38] O. Kalashev, M. Pshirkov, M. Zotov, Identifying nearby sources of ultra-high-energy cosmic rays with deep learning (2019) arXiv:[1912.00625](https://arxiv.org/abs/1912.00625).
- [39] M. Erdmann, L. Geiger, D. Schmidt, M. Urban, M. Wirtz, Origins of extragalactic cosmic ray nuclei by contracting alignment patterns induced in the galactic magnetic field, *Astropart. Phys.* 108 (2019) 74–83, doi:[10.1016/j.astropartphys.2018.11.004](https://doi.org/10.1016/j.astropartphys.2018.11.004).
- [40] M. Abadi, et al., Tensorflow: Large-scale machine learning on heterogeneous distributed systems, *CoRR* (2016) arXiv:[1603.04467](https://arxiv.org/abs/1603.04467).
- [41] Y. Wang, Y. Sun, Z. Liu, S.E. Sarma, M.M. Bronstein, J.M. Solomon, Dynamic graph CNN for learning on point clouds, *CoRR* (2018) arXiv:[1801.07829](https://arxiv.org/abs/1801.07829).
- [42] H. Qu, L. Gouskos, ParticleNet: jet tagging via particle clouds, *Phys. Rev. D* 101 (5) (2020) 056019, doi:[10.1103/PhysRevD.101.056019](https://doi.org/10.1103/PhysRevD.101.056019).
- [43] G. Kasieczka, T. Plehn, et al., The machine learning landscape of top taggers, *SciPost Phys.* 7 (2019) 14, doi:[10.21468/SciPostPhys.7.1.014](https://doi.org/10.21468/SciPostPhys.7.1.014).
- [44] M.S. Pshirkov, P.G. Tinyakov, P.P. Kronberg, K.J. Newton-McGee, Deriving global structure of the Galactic Magnetic Field from Faraday Rotation Measures of extragalactic sources, *Astrophys. J.* 738 (2011) 192, doi:[10.1088/0004-637X/738/2/192](https://doi.org/10.1088/0004-637X/738/2/192).
- [45] R. Jansson, G.R. Farrar, A new model of the galactic magnetic field, *Astrophys. J.* 757 (2012) 14, doi:[10.1088/0004-637X/757/1/14](https://doi.org/10.1088/0004-637X/757/1/14).
- [46] M.S. Pshirkov, P.G. Tinyakov, F.R. Urban, Mapping UHECRs deflections through the turbulent galactic magnetic field with the latest RM data, *Mon. Not. Roy. Astron. Soc.* 436 (2013) 2326, doi:[10.1093/mnras/stt1731](https://doi.org/10.1093/mnras/stt1731).
- [47] R. Jansson, G.R. Farrar, The galactic magnetic field, *Astrophys. J.* 761 (2012) L11, doi:[10.1088/2041-8205/761/1/L11](https://doi.org/10.1088/2041-8205/761/1/L11).
- [48] M.C. Beck, A.M. Beck, R. Beck, K. Dolag, A.W. Strong, P. Nielaba, New constraints on modelling the random magnetic field of the MW, *JCAP* 1605 (05) (2016) 056, doi:[10.1088/1475-7516/2016/05/056](https://doi.org/10.1088/1475-7516/2016/05/056).
- [49] J.L. Han, R.N. Manchester, W. van Straten, P. Demorest, Pulsar rotation measures and large-scale magnetic field reversals in the galactic disk, *Astrophys. J. Suppl. Series* 234 (1) (2018) 11, doi:[10.3847/1538-4365/aa9c45](https://doi.org/10.3847/1538-4365/aa9c45).
- [50] R. Fisher, Dispersion on a Sphere, *Proc. R. Soc. Lond. A* 217 (1130) (1953) 295–305, doi:[10.1098/rspa.1953.0064](https://doi.org/10.1098/rspa.1953.0064).
- [51] S. Ando, A. Kusenko, Evidence for gamma-ray halos around active galactic nuclei and the first measurement of intergalactic magnetic fields, *Astrophys. J. Lett.* 722 (L39) (2010), doi:[10.1088/2041-8205/722/1/L39](https://doi.org/10.1088/2041-8205/722/1/L39).
- [52] F. Fenu, The cosmic ray energy spectrum measured using the Pierre Auger Observatory, [PoSICRC2017,486(2018)] (2017) 9–16, doi:[10.22323/1.301.0486](https://doi.org/10.22323/1.301.0486).
- [53] R. Alves Batista, A. Dundovic, M. Erdmann, K.-H. Kampert, D. Kuempel, G. Müller, G. Sigl, A. van Vliet, D. Walz, T. Winchen, CRPropa 3 – a public astrophysical simulation framework for propagating extraterrestrial ultra-high energy particles, *JCAP* 1605 (05) (2016) 038, doi:[10.1088/1475-7516/2016/05/038](https://doi.org/10.1088/1475-7516/2016/05/038).
- [54] A. Zonca, L. Singer, D. Lenz, M. Reinecke, C. Rosset, E. Hivon, K. Gorski, healpy: equal area pixelization and spherical harmonics transforms for data on the sphere in python, *J. Open Source Softw.* 4 (35) (2019) 1298, doi:[10.21105/joss.01298](https://doi.org/10.21105/joss.01298).
- [55] K.M. Górski, E. Hivon, A.J. Banday, B.D. Wandelt, F.K. Hansen, M. Reinecke, M. Bartelmann, HEALPix: a framework for high-resolution discretization and fast analysis of data distributed on the sphere, *Astrophys. J.* 622 (2005) 759–771, doi:[10.1086/427976](https://doi.org/10.1086/427976).
- [56] P. Sommers, Cosmic ray anisotropy analysis with a full-sky observatory, *Astropart. Phys.* 14 (2001) 271–286, doi:[10.1016/S0927-6505\(00\)00130-4](https://doi.org/10.1016/S0927-6505(00)00130-4).
- [57] N. Chiba, et al., Akeno giant air shower array (AGASA) covering 100 km² area, *Nucl. Instrum. Meth. A* 311 (1992) 338–349, doi:[10.1016/0168-9002\(92\)90882-5](https://doi.org/10.1016/0168-9002(92)90882-5).
- [58] H. Ohoka, S. Yoshida, M. Takeda, Further development of data acquisition system of AGASA, *Nucl. Instrum. Meth. A* 385 (1997) 268–276, doi:[10.1016/S0168-9002\(96\)01027-3](https://doi.org/10.1016/S0168-9002(96)01027-3).
- [59] Institute for Cosmic Ray Research, University of Tokyo, Scientific activities: report to the review committee, 2007. Unpublished.
- [60] M. Takeda, et al., Small-scale anisotropy of cosmic rays above 10¹⁹ eV observed with the Akeno giant air shower array, *Astrophys. J.* 522 (1) (1999) 225–237, doi:[10.1086/307646](https://doi.org/10.1086/307646).
- [61] N. Hayashida, et al., Updated AGASA event list above 4 × 10¹⁹ eV, *Astron. J.* 120 (2000) 2190.
- [62] Y. LeCun, B. J., Convolutional networks for images, speech, and time-series, in: M.A. Arbib (Ed.), *The Handbook of Brain Theory and Neural Networks*, MIT Press, 1995, p. 14.
- [63] N. Perraudin, M. Defferrard, T. Kacprzak, R. Sgier, DeepSphere: efficient spherical convolutional neural network with HEALPix sampling for cosmological applications, *Astron. Comput.* 27 (2019) 130–146, doi:[10.1016/j.ascom.2019.03.004](https://doi.org/10.1016/j.ascom.2019.03.004).
- [64] W.L. Hamilton, R. Ying, J. Leskovec, Representation learning on graphs: Methods and applications, *CoRR* (2017) arXiv:[1709.05584](https://arxiv.org/abs/1709.05584).
- [65] T.N. Kipf, M. Welling, Semi-supervised classification with graph convolutional networks (2016) arXiv:[1609.02907](https://arxiv.org/abs/1609.02907).
- [66] D.P. Kingma, J. Ba, Adam: A Method for Stochastic Optimization (2014) arXiv:[1412.6980](https://arxiv.org/abs/1412.6980).
- [67] L. van der Maaten, G. Hinton, Visualizing high-dimensional data using t-SNE, *J. Mach. Learn. Res.* 9 (Nov) (2008) 2579–2605, <https://www.jmlr.org/papers/volume9/vandermaaten08a/vandermaaten08a.pdf>.
- [68] P. Abreu, et al., Bounds on the density of sources of ultra-high energy cosmic rays from the Pierre Auger Observatory, *J. Cosmol. Astropart. Phys.* 2013 (05) (2013) 009, <https://iopscience.iop.org/article/10.1088/1475-7516/2013/05/009>.
- [69] A. Cuoco, S. Hannestad, T. Haugbølle, M. Kachelrieß, P.D. Serpico, A global autocorrelation study after the first Auger data: impact on the number density of UHECR sources, *Astrophys. J.* 702 (2) (2009) 825–832, <https://iopscience.iop.org/article/10.1088/0004-637X/702/2/825/meta>.